Available online at www.sciencedirect.com
ScienceDirect
Trans. Nonferrous Met. Soc. China 27(2017) 2225−2233
Transactions of Nonferrous Metals Society of China
www.tnmsc.cn

Microstructural, corrosion and mechanical behavior of two-step plasma electrolyte oxidation ceramic coatings

H. KHANMOHAMMADI, S. R. ALLAHKARAM, N. TOWHIDI

Mechanically Assisted Corrosion Laboratory, School of Metallurgy and Materials Engineering, College of Engineering, University of Tehran, P. O. Box 11155-4563 Tehran, Iran

Received 9 August 2016; accepted 23 January 2017

Abstract: Plasma electrolytic oxidation (PEO) is considered as a cost effective and environmentally friendly surface treatment process for improving surface properties of light alloys. The formation of ceramic coatings on Ti6Al4V alloy was reported by two-step PEO process and its structural, electrochemical and mechanical properties with the coated samples were compared by one-step PEO process in an alkaline electrolyte. The structural properties were studied using field-emission scanning microscope (FESEM) and X-ray diffraction (XRD). Electrochemical studies were carried out using linear polarization method and in addition mechanical behaviors were investigated by means of Knoop microhardness and nanoindentation method. Results showed that the second step process resulted in an increase of both porosity percentage and average pore diameter on the surface. The two-step process resulted in a small increase of thickness from about 12.5 to 13.0 μm. Electrochemical test results showed that applying the second step resulted in the decrease of both polarization resistance from 1800.2 to 412.5 kΩ/cm^2 and protection efficiency from 97.8% to 90.5%. Finally, the nanoindentation results indicated that the PEO coatings became softer but more ductile after applying the second processing step in acidic electrolyte.

Key words: plasma electrolytic oxidation; microstructure; corrosion; nanoindentation

1 Introduction

Titanium and its alloys are widely used in different industries such as aerospace, marine and biomedicine. This broad range of application of these alloys is due to their high specific strength, good corrosion behavior and biocompatibility [1−5]. On the other hand, low surface hardness and weak wear behavior limit their usage in tribological applications [6,7]. Therefore, different surface treatment processes have been developed for improving the tribological behavior of this group of alloys (i.e. anodizing, chemical vapor deposition (CVD), physical vapor deposition (PVD), ion implantation and laser nitriding [8,9]).

Plasma electrolytic oxidation (PEO) which is also called micro-arc oxidation [1,10,11] is a relatively new surface engineering process to apply ceramic-like coatings on light alloys such as titanium, magnesium, aluminium and zirconium [12−16]. Applying the oxide coatings by this method can enhance the corrosion behavior [17−20], but there are limited studies on the mechanical properties of these coatings [21]. The general mechanism of PEO process (regardless of type of substrate, chemical composition of electrolyte and electrical parameters of process) can be summarized as follows:

1) Formation of a thin natural passive film on the surface;

2) Production of gas bubbles on the surface which results in the growth of a porous film with a columnar structure perpendicular to the surface;

3) Start of micro-discharging when the voltage exceeds the intrinsic breakdown voltage of the oxide film on the surface [10];

4) Formation of plasma atmosphere in electrolyte near to the interface of electrolyte−anode which results in ionization of some elements of electrolyte and entrance of these ions into the coating.

Two-step plasma electrolyte oxidation, which consists of a primary PEO process in alkaline electrolytes and a final short-time PEO process in acidic electrolytes, was proposed by some researchers to achieve better adhesion of coating to substrate [22] and

Corresponding author: S. R. ALLAHKARAM; Tel: +98-21-61114108; E-mail: akaram@ut.ac.ir
DOI: 10.1016/S1003-6326(17)60248-6

higher corrosion resistance of the coatings [23].

Nanoindentation is a mechanical characterization method for thin film systems and small volumes of materials [24]. Usually, the principal goal of such testing is to obtain elastic modulus and hardness of the specimen. The forces involved in this method are usually in the millinewton range and were measured with a resolution of a few nanonewtons. The depth of penetration is in the order of nanometers [24,25].

In the present study, one-step and two-step PEO coatings on the surface of Ti−6Al−4V alloy were prepared and the effect of the second step on the microstructure, corrosion resistance and mechanical behavior of the coatings was discussed.

2 Experimental

2.1 Substrate preparation

In this study, Ti6Al4V titanium alloy was used as substrate. The samples were cut in the shape of disks with 30 mm in diameter and 4 mm in thickness. The disks were ground with SiC abrasive paper (60−1500#), then polished by alumina nanoparticle suspension and at the end washed with distilled water and acetone.

2.2 PEO process

A bipolar pulse galvanostatic power supply was employed for plasma electrolyte oxidation. Two different electrolytes were used in this study: an alkaline electrolyte (based on our previous study on the effect of electrolyte chemical composition [26]) containing sodium aluminate (15 g/L $Na_2Al_2O_4$), sodium phosphate (2 g/L Na_3PO_4) and sodium fluoride (1.5 g/L NaF) and an acidic electrolyte used in two-step PEO process (containing 0.1 mol/L H_2SO_4 and 0.1 mol/L H_3PO_4) [22]. The applied current density, positive duty cycle, negative duty cycle and frequency were designated to be 0.12 A/cm^2, 50%, 25% and 1000 Hz, respectively. Temperature of the electrolyte was kept below 25 °C using a cooling system as shown in Fig. 1. Table 1 summarizes the processing steps to achieve the coatings.

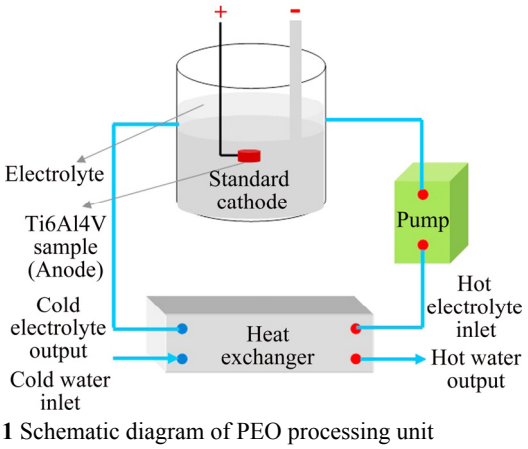

Fig. 1 Schematic diagram of PEO processing unit

Table 1 Processing electrolytes and duration time of different steps

Sample	Step 1		Step 2	
	Electrolyte	Time/s	Electrolyte	Time/s
1S	Alkaline	360	−	−
2S	Alkaline	360	Acidic	30

* In all tests, current density, positive and negative duty cycles and frequency of the PEO process were 0.12 A/cm^2, 50%, 25% and 1000 Hz, respectively.

2.3 Microstructure

The cross-section samples were mounted and ground with SiC emery papers up to 4000# and then were polished using alumina nanoparticle suspension. Surface morphology and cross-section images of the coatings were examined using a scanning electron microscope (SEM, JEOL6300). All the samples were coated with about 50 nm gold layer to avoid surface charging. The thickness of the coatings was measured using cross-section SEM images. The obtained surface morphology images were processed by means of Image Processing Lab software to estimate the surface porosity and the average porosity diameter on the surface of each coating. Chemical composition on the surface and on different parts of the cross-sectional samples was investigated via energy dispersive spectrometer (EDS). Phase composition of the coatings was also analyzed by means of X-ray diffractometer (XRD, Philips X'Pert, with Cu K_α radiation by scanning in the range of 2θ=10°−90°).

2.4 Mechanical properties

Hardness and elastic modulus of the coatings and the substrate have been obtained by nanoindentation test from the cross-sectional samples. All nanoindentation tests were carried out using a Nanoindentor G200 Agilent Technologies. A Berkovich diamond tip was used, whose area function was calibrated in a pattern of fuse silica. The nanoindenting process was carried out on 25 different points on the samples and the average value was reported. Each nanoindentation test was performed with maximum penetration depth of 400 nm. The nanohardness and elastic modulus of each coating were plotted versus penetration depth. The effect of substrate on nanoindentation data of coatings could be considered negligibly if each edge of the indentation track was smaller than 10% of the thickness of the coatings [24]. Equation (1) shows the relationship between the projected area of nanoindentation (A) and penetration depth (h) [24].

$$A = 3\sqrt{3}h^2 \tan^2\theta \quad (1)$$

The value of θ is 65.27° based on the geometry of

Berkovich indenter. Hence,

$$A=24.49h^2 \quad (2)$$

On the other hand, based on the fact that the projected area with Berkovich indenter is equilateral triangle, the equation between each side of this triangle (x) and the projected area (A) is as Eq. (3):

$$A=\frac{\sqrt{3}}{4}x^2 \quad (3)$$

After putting the area (A) as a function of x in Eq. (2), we have

$$h=0.133x \quad (4)$$

Based on Eq. (4), for a coating with the thickness of about 12 μm, x is smaller than 1.2 μm or 1200 nm. Hence, the maximum penetration depth must be about 160 nm. Based on these calculations, real nanohardness and elastic modulus of the coatings were measured as the average value of them between the penetration depths of 40 and 160 nm.

The mechanical properties of the coatings were measured using continuous stiffness technique [24,25]. The energy loss through plastic deformation (W_p) was calculated from the area enclosed by the loading and unloading curves of the load−displacement graphs. This W_p is considered to be a measure of fracture toughness of the coatings (ignoring other energy dissipative phenomena), as illustrated in Fig. 2 [24,25].

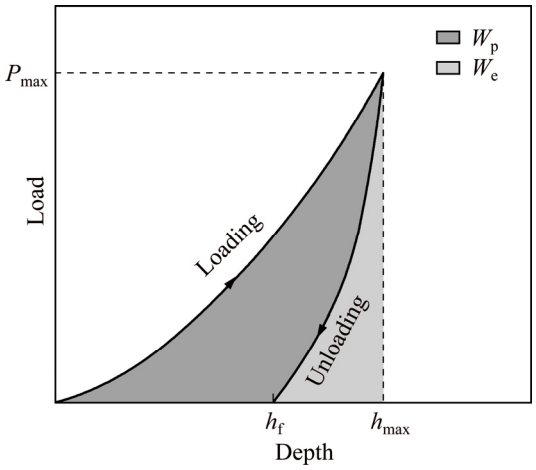

Fig. 2 Energy lost through plastic (W_p) and elastic (W_e) deformation [24,25]

The pyramidal geometry of Knoop indenter makes it an appropriate indenter to measure microhardness of brittle materials and thin films [25]. Microhardness measurements of the coatings were carried out using a Knoop indenter under different loads of 10, 25 and 50 g.

2.5 Corrosion behavior

Potentiodynamic polarization tests were carried out using a BioLogic SP−150 potentiostat/galvanostat on all coated samples and on the uncoated Ti−6Al−4V substrate. A Ag/AgCl (3 mol/L KCl) electrode was used as a reference electrode (whose difference is 205 mV with respect to SHE) and a platinum foil (1 cm^2) was used as a counter electrode. Prior to the potentiodynamic tests, open circuit potential (OCP) of the samples was measured for 60 min. Potentiodynamic polarization tests were carried out between −300 and 700 mV with respect to the OCP, at a scan rate of 1 mV/s. All tests were repeated at least twice to check for reproducibility.

3 Results and discussion

3.1 Structural properties

Figure 3 shows the XRD patterns of one-step (1S) and two-step (2S) PEO coatings. Due to the low thickness of the coatings, strong peaks related to the titanium based substrate are observable.

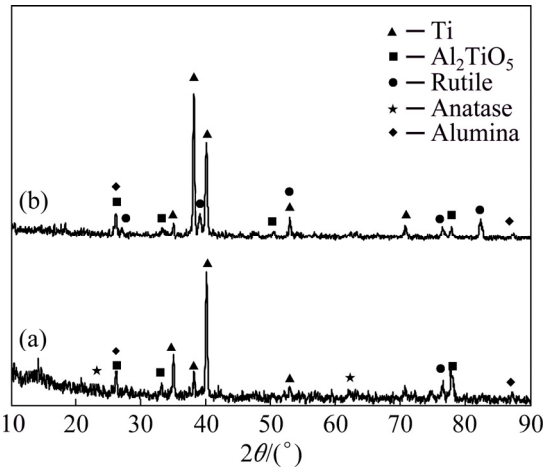

Fig. 3 XRD patterns of one-step (a) and two-step (b) coatings

Alumina, two different titanium oxide phases (anatase and rutile) and a titanium−aluminium complex oxide phase (Al_2TiO_5) are the main phases in 1S. On the other hand, peaks of anatase are not detectable in the XRD pattern of 2S. This can be attributed to the fact that at higher temperatures the phase transformation of anatase to rutile takes place and the higher temperature of the second step of processing can supply the required energy for this phase transformation [1,14]. Moreover, the high temperature of micro-sparks during the second step can facilitate the formation of Al_2TiO_5 in accordance to the Reaction 5 [14]:

$$TiO_2+Al_2O_3 \rightarrow Al_2TiO_5 \quad (5)$$

Based on the mentioned facts, the presence of higher amounts of rutile and Al_2TiO_5 in 2S sample (as

the sharper peaks of these phases in XRD pattern of 2S are observable) can be explained.

Figure 4 shows the surface morphology and image-processed files of surface SEM images of the coatings. The coatings contain different porosity percentages with different average pore sizes on their surfaces. The total porosity and total quantity of pores of each sample were determined from the image processed SEM micrographs for a surface area of 41 μm × 41 μm. Based on the obtained data the average pore area (S_p) on the surface of each sample can be calculated by dividing the total porosity area to total number of pores (n). Moreover, the average pore diameter (d) can be calculated by

$$d = \sqrt{\frac{4S_p}{\pi n}} \tag{6}$$

The surface chemical composition of the coatings was characterized by EDS from five 10 μm × 10 μm random areas on the surface of each sample. The chemical composition (Al/Ti value), porosity and the average pore diameter on the surface of the coatings are shown in Table 2.

The w(Al)/w(Ti) represents the mass ratio of Al and Al−Ti complex oxides (Al_2O_3 and Al_2TiO_5) to pure TiO_2 on the surface of the coatings. Table 2 shows that the w(Al)/w(Ti) value of 2S is higher than 1S. Some researchers showed that the increase in absorption of metallic ions from electrolyte (i.e. aluminum ions in aluminate-base electrolyte), is due to formation of larger sparks during the macro-sparking process [27,28]. Larger arcs lead to higher amount of molten metal and large amount of molten metals can absorb more metallic ions from the electrolyte. In aluminate-base electrolytes, severe arcs during the second step of PEO processing can result in absorption of more aluminum ions from the electrolyte and higher Al/Ti mass ratios on the surface of the coating.

As it can be seen in Table 2, the second step of PEO process resulted in higher porosity (about 6 times higher) and larger average pore diameter (about twice larger) of 2S compared with 1S. This can be due to the larger and more severe arcs during the second step of processing in the acidic electrolyte.

Figure 5 shows the cross-section SEM images of the samples. Table 3 represents the thickness of the coatings and the chemical composition in different depths of the coatings (different points of EDS measurements are specified in Fig. 5).

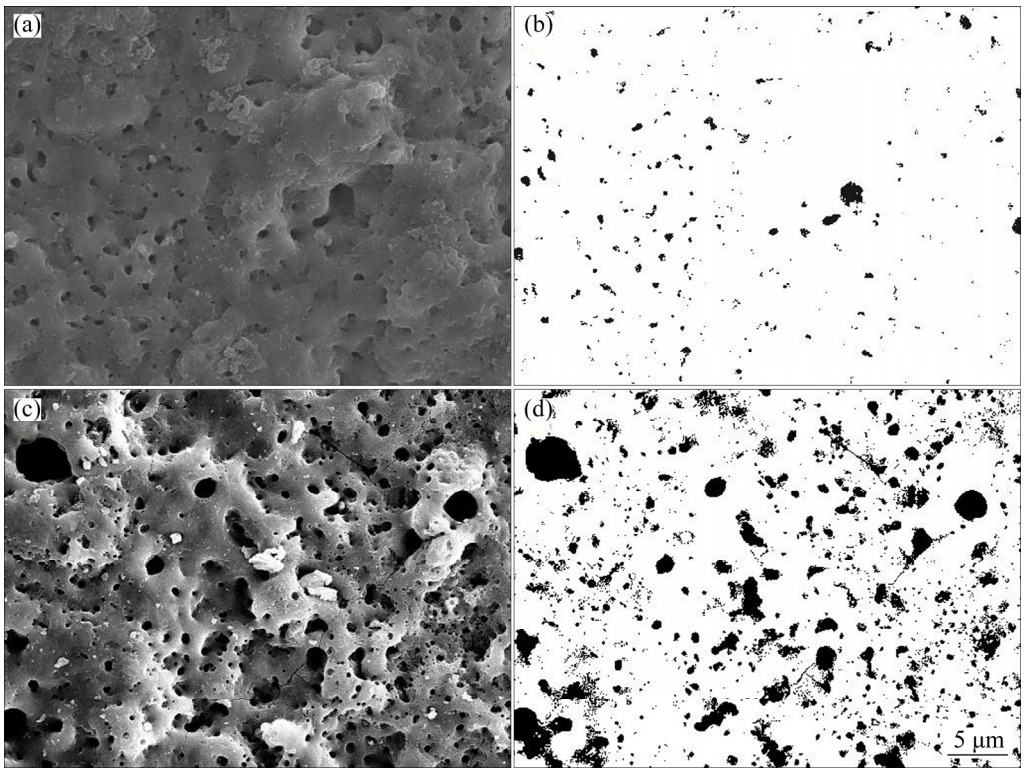

Fig. 4 Surface morphologies (a, c) and image-processed micrographs (b, d) of 1S (a,b) and 2S (c,d)

Table 2 Porosity and chemical composition of coatings

Sample	w(Al)/%	w(Ti)/%	w(Al)/w(Ti)	Porosity/%	Average pore
1S	29.8±1.7	26.2±1.5	1.14±0.09	2.7±0.6	0.66±0.07
2S	34.5±2.9	20.9±2.2	1.65±0.10	16.2±3.5	1.21±0.16

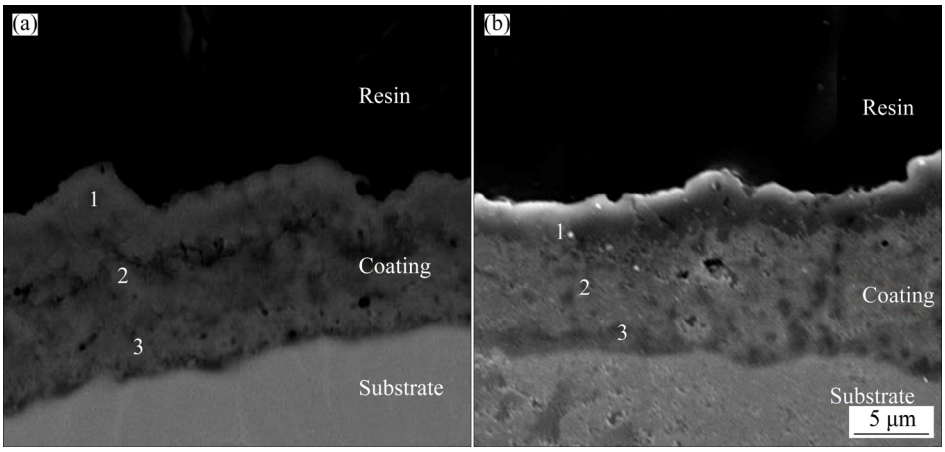

Fig. 5 Cross-section SEM images of 1S (a) and 2S (b)

Table 3 Chemical composition of different points on cross-section of coatings

Sample	Position 1			Position 2			Position 3			Thickness/ μm
	w(Al)/%	*w*(Ti)/%	*w*(Al)/*w*(Ti)	*w*(Al)/%	*w*(Ti)/%	*w*(Al)/*w*(Ti)	*w*(Al)/%	*w*(Ti)/%	*w*(Al)/*w*(Ti)	
1S	39.5±4.1	15.2±1.2	2.6±0.1	31.2±2.9	19.1±2.0	1.6±0.1	20.0±1.1	35.6±2.1	0.6±0.0	12.5 ± 2.1
2S	41.9±3.9	12.0±1.0	3.5±0.2	34.6±3.0	20.0±1.8	1.7±0.1	11.1±0.8	45.2±4.1	0.3±0.0	12.9 ± 1.0

As can be seen in Fig. 5 and Table 3, there is no large difference between the thicknesses of 1S and 2S. Therefore, it can be deduced that the second step PEO in acidic electrolyte did not affect the thickness efficiently. Above mentioned phenomenon can be due to the weak discharges during the second step of PEO processing and this is in agreement with previous studies [22,29]. The chemical composition data reveal that Al/Ti mass ratio on the surface of 2S (point 1 in Fig. 5(b)) is higher than that on the surface of 1S (point 1 in Fig. 5(a)). As mentioned before, it can be due to the higher absorption of aluminum ions from the electrolyte by larger macro-discharges during the second step. On the other hand, Table 3 shows that Al/Ti mass ratio in regions near to the interface of the coating and substrate of 1S (point 3 in Fig. 5(a)) is higher than that in 2S (point 3 in Fig. 5(b)). Some other studies [22,29,30] showed that during the second step of PEO process in acidic electrolyte, discharges are focused on the columnar structure of the pores and the main process (during the second step) occurs near the interface of substrate−coating and can fill in some of the pores and voids close to this interface. According to the findings of these reports, phases that are formed close to the substrate−coating contain mostly oxides of the elements of the substrate. Hence, the second PEO step in acidic electrolyte leads to titanium enrichment in the inner regions of the coatings.

3.2 Mechanical properties

Figure 6 shows the hardness and elastic modulus of PEO-coated samples and the Ti−6Al−4V substrate versus the penetration depth.

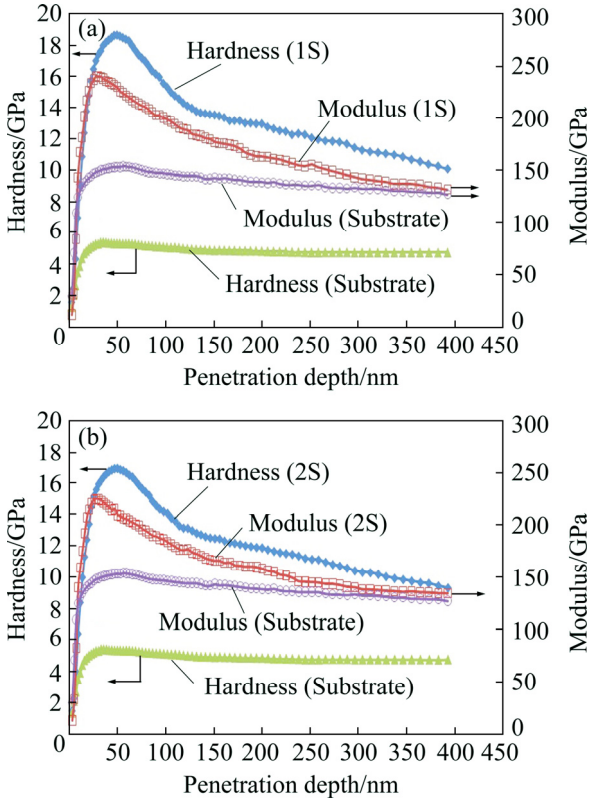

Fig. 6 Nanohardness and modulus versus penetration depth of 1S and substrate (a) and 2S and substrate (b)

The hardness and elastic modulus of the substrate are more or less constant after the first 30 nm that can be due to the homogeneity of the alloy in different penetration depths but the hardness and modulus of the coatings are not constant because of the effect of substrate in larger penetration depths. The elastic

modulus reveals that the elastic behavior of the coatings in depth deeper than about 300 nm is the same as that of the substrate. On the other hand, the plastic behavior (hardness) of the coatings is completely different with that of the substrate along 400 nm penetration. Based on the contact mechanics, the elastically affected volume beneath the contact point is larger than the plastically affected volume [31]. In other words, the effect of mechanical properties of the substrate on elastic modulus is detectable in lower depths compared with that of the substrate on the hardness.

Table 4 shows the average hardness and elastic modulus of the coatings and the substrate and the energy of plastic deformation derived from load−displacement curves of 1S and 2S.

Table 4 Hardness, modulus and plastic energy derived from nanoindentation tests

Sample	Nanohardness/GPa	Modulus/GPa	W_p/(mN·nm)
Substrate	5.1±0.1	148.0±1.2	–
1S	16.1±0.4	197.4±4.3	263±7
2S	14.7±0.5	189.2±5.3	317±10

It can be concluded that the second step of PEO processing in acidic electrolyte has led to a decrease in hardness and an increase in plastic energy. As it mentioned before, by ignoring some probable energy dissipative phenomena, the energy loss during plastic deformation can be a measure of toughness. TSUNEKAWA et al [22] showed that the light emission during the second step is lower and the arcs are integrated in limited points on the surface. These limited but powerful arcs during the second step can act as a heat treatment source for other parts of the coating. In other words, the second PEO step can cause tempering of the oxide layer that leads to decrease in hardness which can in turn increase the toughness. It should be mentioned that these severe arcs during the second step act along the pore channels [22,29,30] and hence can cause some phase transformations in substrate as well.

Figure 7 shows the Knoop microhardness data of the coatings at different normal loads on the indenter. It can be seen that at higher loads (25 and 50 g) the microhardnesses of the coatings are the same and very near to that of the substrate. Hence, at normal loads (higher than 10 g), the plastic deformation affected volume contains the substrate. On the other hand, the measurements under the load of 10 g are in accordance with the nanoindentation data and show about 10% decrease in hardness after applying the second PEO step.

3.3 Corrosion behavior

An oxide film by limiting adsorption of corrosive ions causes a shift in surface electrochemical potential and a reduction in the charge-carrier mobility at the surface−electrolyte interface, which in turn, protects the substrate from corrosion. Corrosion behavior of the oxide-based coatings is affected by a combination of characteristics of the oxide film (e.g. chemical composition, phase composition, porosity and structural imperfections and thickness) and corrosion environment (such as concentration of aggressive ions and temperature) [2,26].

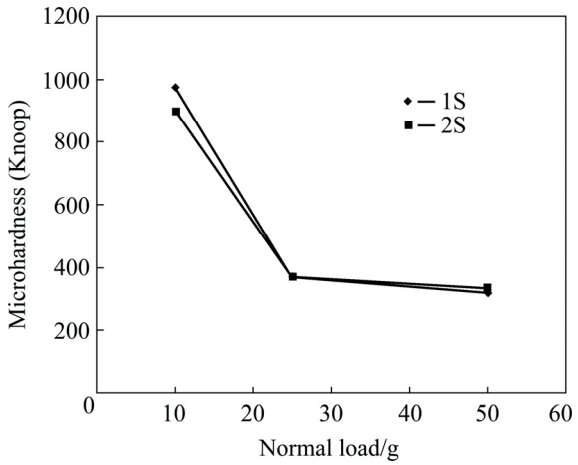

Fig. 7 Knoop microhardness of coatings at different normal loads

Large micropores on the surface of PEO coatings increase the real area that exposed to the corrosive solution. On the other hand, an increase in coating thickness increases the barrier property of the coating and improves the corrosion behavior [26].

Tafel curves of the untreated Ti−6Al−4V substrate and the coatings are shown in Fig. 8. The Stern−Geary equation was used to obtain polarization resistance (R_p) [1].

$$R_p = \frac{\beta_a \beta_c}{2.303(\beta_a + \beta_c) J_{corr}} \quad (7)$$

where β_a and β_c are anodic and cathodic Tafel constants and J_{corr} is the corrosion current density.

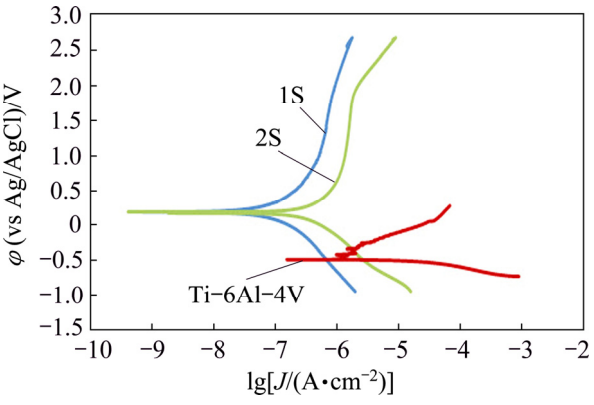

Fig. 8 Tafel curves of substrate and coatings

The protection efficiency (η) of the coatings was calculated using the following formula:

$$\eta = \frac{R_p^{coat} - R_p^{sub}}{R_p^{coat}} \times 100\% \quad (8)$$

The corrosion potential (φ_{corr}), the corrosion current density (J_{corr}), the polarization resistance (R_p) and the protection efficiency of the coatings obtained from the polarization curves are shown in Table 5.

Table 5 Electrochemical data of samples derived from linear polarization curves

Sample	φ_{corr}(vs Ag/AgCl)/V	J_{corr}/ (A·cm^{-2})	R_p/ (kΩ·cm^{-2})	Protection efficiency/%
Ti−6Al−4V	−0.50±0.02	0.877±0.013	39.3±0.6	−
1S	+0.19±0.02	0.016±0.001	1800.2±1.3	97.8
2S	+0.17±0.01	0.173±0.004	412.5±1.0	90.5

Comparing the polarization curves of the substrate and the coatings in Fig. 8 shows four obvious outcomes.

1) The corrosion potentials of the coatings (0.19 V for 1S and 0.17 V for 2S) are more positive compared with that of the Ti−6Al−4V substrate (−0.50 V). This shows the lower thermodynamic driving force for the corrosion of the coatings.

2) The corrosion potential of 2S is more negative than that of 1S. This is due to an increase in surface porosity during the second step and higher amount of diffusion free paths for corroding ions on the structure of 2S.

3) The corrosion current densities of the PEO-coated samples are lower than that of the substrate. This implies that the anodic reactions were prevented by PEO process and a higher chemical stability is obtained on the surface of the coated samples.

4) The second step of PEO process makes the corrosion current density increase by one order of magnitude (from 0.016 to 0.173 μA). Moreover, the protection efficiency of 2S is 7.3% lower than that of 1S. This decrease in corrosion behavior can be related to the increase in both the porosity and the average pore diameter of 2S compared with 1S (Table 2).

Based on the assumption that the ceramic coating is electrochemically inert at low anodic overpotentials, the porosity of the coating can be calculated as [32]

$$P = \frac{R_{ps}}{R_{pc}} \times 10^{-(\Delta\varphi_{corr}/\beta_{as})} \times 100\% \quad (9)$$

where P is the total porosity, R_{ps} is the polarization resistance of the substrate, R_{pc} is the polarization resistance of the coating, $\Delta\varphi_{corr}$ is the difference between the corrosion potentials of the coating and the substrate and β_{as} is the anodic slop of the Tafel curve of the substrate. Based on the formula (9), the ratio of the porosity of 2S to that of 1S can be calculated as

$$\frac{P_{2S}}{P_{1S}} = \frac{R_p^{1S}}{R_p^{2S}} \times 10^{\left(\frac{\varphi_{corr}^{1S} - \varphi_{corr}^{2S}}{\beta_a}\right)} \quad (10)$$

By applying the data derived from the Tafel extrapolations and 0.4 for the anodic slope of the substrate, the P_{2S}/P_{1S} ratio will be 3.89:1. On the other hand, the P_{2S}/P_{1S} ratio calculated from the processed SEM images (Table 2) is about 6:1. The difference between the two ratios can be due to the fact that the porosity derived from the SEM images is the surface porosity (that may be open or closed) and the data derived from the electrochemical measurements are about the open porosities that corrosive ions can penetrate through them to the substrate.

4 Conclusions

1) Applying the second step of PEO process in acid electrolyte significantly affects the microstructure, chemical and phase composition of the coating. Two-step PEO processing leads to higher porosity and larger pore diameter on the surface. Moreover, the aluminium content of the two-step coating is higher than that of the one-step sample as a result of severe macro-sparks during the second step and absorbing more aluminium ions from the aluminate-base electrolyte. On the other hand, high temperature during the second step (as a result of severe macro-arcs) results in activation of high-temperature phase transformation and thus, higher amount of Al_2TiO_5 complex oxide phase.

2) Two-step PEO processing results in about 9% decrease in nanohardness (from 16.1 to 14.7 GPa) but about 20% increase in energy loss through plastic deformation that can be concluded as an increase in fracture toughness.

3) The corrosion resistance increases drastically by applying ceramic-like coatings via PEO process. Applying the second step of PEO process results in a decrease in corrosion resistance, an increase in corrosion current density and a shift of the corrosion potential to more negative values. This can be attributed to the higher porosity and larger average pore diameter on the surface of the two-step sample compared with the single-step sample.

Acknowledgment

The authors would like to thank International affairs department of University of Tehran and Sarkhoon & Qeshm Gas Treating Company for the financial support of this study.

References

[1] SHOKOUHFAR M, DEHGHANIAN C, MONTAZERI M, BARADARAN A. Preparation of ceramic coating on Ti substrate by plasma electrolyte oxidation in different electrolytes and evaluation of its corrosion resistance: Part II [J]. Applied Surface Science, 2012, 258: 2416−2423.

[2] YEROKHIN A L, NIE X, LEYLAND A, MATTHEWS A, Characterization of oxide films produced by plasma electrolyte oxidation of a Ti−6Al−4V alloy [J]. Surface and Coatings Technology, 2000, 130: 195−206.

[3] WANG Y, JIANG B, LEI T, GUO L, Dependence of growth features of microarc oxidation coatings of titanium alloy on control modes of alternate pulse [J]. Materials Letters, 2004, 58: 1907−1911.

[4] FEI C, HAI Z, CHEN C, YANG J X, Study on the tribological performance of ceramic coatings on titanium alloy surfaces obtained through microarc oxidation [J]. Progress in Organic Coatings, 2009, 64: 264−267.

[5] HUANG P, WANG F, XU K, HAN Y. Mechanical properties of titania prepared by plasma electrolyte oxidation [J]. Surface and Coatings Technology, 2007, 201: 5168−5171.

[6] KUROMOTO N K, SIMAO R A, SOARES G A. Titanium oxide films produced on commercially pure titanium by anodic oxidation with different voltages [J] Materials Characterization, 2007, 58: 114−121.

[7] MU M, LIANG J, ZHOU X, XIAO Q, One-step preparation of TiO_2/MoS_2 composite coating on Ti6Al4V alloy by plasma electrolyte oxidation and its tribological properties [J]. Surface and Coatings Technology, 2013, 214: 124−130.

[8] CHENG T, CHEN Y, NIE X, Surface morphology manipulation and wear property of bioceramic oxide coatings on titanium alloy [J]. Surface and Coatings Technology, 2013, 215: 253−259.

[9] NIE X, LEYLAND A, MATTHEWS A. Low-temperature deposition of $Cr(N)/TiO_2$ coatings using a duplex process of unbalanced magnetron sputtering and micro-arc oxidation [J]. Surface and Coatings Technology, 2000, 133: 331−337.

[10] JAVIDI M, FADAEE H. Plasma electrolytic oxidation of 2024-T3 aluminum alloy and investigation on microstructure and wear behavior [J]. Applied Surface Science, 2013, 286: 212−219.

[11] XIANG N, SONG R G, ZHUANG J J, SONG R X, LU X Y, SU X P. Effects of current density on microstructure and properties of plasma electrolytic oxidation ceramic coatings formed on 6063 aluminum alloy [J] Transactions of Nonferrous Metals Society of China, 2016, 26: 806−813.

[12] BARATI N, MELETIS E I, GHOLESTANI-FARD F, YEROKHIN A, RASTEGARI S, FAGHIHI-SANI M A. $Al_2O_3−ZrO_2$ nanostructured coatings using DC plasma electrolyte oxidation to improve tribological properties of Al substrates [J]. Applied Surface Science, 2015, 356: 927−934.

[13] ALIASGHARI S, SKELDON P, THOMPSON G E. Plasma electrolytic oxidation of titanium in a phosphate/silicate electrolyte and tribological performance of the coating. [J]. Applied Surface Science, 2014, 316: 463−476.

[14] SHOKOUHFAR M, ALLAHKARAM S R. Formation mechanism and surface characterization of ceramic composite coatings on pure titanium by microarc oxidation in electrolytes containing nanoparticles [J]. Surface and Coatings Technology, 2016, 291: 396−405.

[15] WANG K, KOO B H, LEE C G, KIM Y J, LEE S H, BYON E, Effects of electrolytes variation on formation of oxide layers of 6061 Al alloys by plasma electrolytic oxidation [J]. Transactions of Nonferrous Metals Society of China, 2009, 19: 866−870.

[16] CENGIZ C, GENCER Y. The characterization of the oxide based coating synthesized on pure zirconium by plasma electrolyte oxidation [J]. Surface and Coatings Technology, 2014, 242: 132−140.

[17] KUMAR A M, KWON S, JUNG H C, SHIN K S. Corrosion protection performance of single and dual plasma electrolyte oxidation (PEO) coating for aerospace applications [J]. Materials Chemistry and Physics, 2015, 149: 480−486.

[18] DENG H, MA Z, ZHANG X, ZHANG Y, LIU X, Corrosion resistance in simulated DMFC environment of plasma electrolyte oxidation coating prepared on aluminum alloy [J]. Surface and Coatings Technology, 2015, 269: 108−113.

[19] HESSEIN R O, NORTHWOOD D O, NIE X, The effect of processing parameters and substrate composition on the corrosion resistance of plasma electrolyte oxidation (PEO) coated magnesium alloys [J]. Surface and Coatings Technology, 2013, 237: 357−368.

[20] CHO J Y, HWANG D Y, LEE D H, YOO B, SHIN D H. Influence of potassium pyrophosphate in electrolyte on coated layer of AZ91 Mg alloy formed by plasma electrolytic oxidation [J]. Transactions of Nonferrous Metals Society of China, 2009, 19: 824−828.

[21] WHITE L, KOO Y, NERALLA S, SANKAR J, YUN Y. Enhanced mechanical properties and increased corrosion resistance of a biodegradable magnesium alloy by plasma electrolyte oxidation (PEO) [J]. Materials Science and Engineering B, 2016, 208: 39−46.

[22] TSUNEKAWA S, AOKI Y, HABAZAKI H. Two-step plasma electrolyte oxidation of Ti−15V−3Al−3Cr−3Sn for wear-resistant and adhesive coating [J]. Surface and Coatings Technology, 2011, 205: 4732−4740.

[23] EINKHAH F, LEE K M, FAGHIHI-SANI M, YOO B, SHIN D H. Structure and corrosion behavior of oxide layer with Zr compounds on AZ31 Mg alloy processed by two-step plasma electrolyte oxidation [J]. Surface and Coatings Technology, 2014, 238: 75−79.

[24] FISCHER-CRIPPS A C, Nanoindentation [M]. 3rd ed. New South Wales, Australia: Springer, 2011.

[25] DEY A, MUKHOPADHYAY A K, Nanoindentation of brittle solids [M]. Boca Raton, Florida, USA: CRC Press, 2014.

[26] KHANMOHAMMADI H, ALLAHKARAM S R, TOWHIDI N, RASHIDFAROKHI A R. Preparation of PEO coating on Ti6Al4V in different electrolytes and evaluation of its properties [J]. Surface Engineering, 2016, 32: 448−456.

[27] YAO Z, JIANG Z, WANG F, HAO G, Oxidation behavior of ceramic coatings on Ti−6Al−4V by microarc oxidation [J]. Materials Processing Technology, 2007, 190: 117−122.

[28] KHORASANIAN M, DEHGHAN A, SHARIAT M H, BAHROLOLOOM M E, JAVADPOUR S. Microstructure and wear resistance of oxide coatings on Ti−6Al−4V produced by plasma electrolyte oxidation in an inexpensive electrolyte [J]. Surface and Coatings Technology, 2011, 206: 1495−1502.

[29] SAH S P, AOKI Y, HABAZAKI H. Influence of phosphate concentration on plasma electrolyte oxidation of AZ80 magnesium alloy in alkaline aluminate solution [J]. Materials Transactions, 2010, 51: 94−102.

[30] HABAZAKI H, ONODERA T, FUSHIMI K, KONNO H, TOYOTAKE K. Spark anodizing of β-Ti alloy for wear-resistant coating [J]. Surface and Coatings Technology, 2007, 201: 8730−8737.

[31] ARCHARD J F. Contact and rubbing of flat surfaces [J]. Applied Physics, 1953, 24: 981−988.

[32] CREUS J, MAZILLE H, IDRISSI H. Porosity evaluation of protective coatings onto steel, through electrochemical techniques [J]. Surface and Coatings Technology, 2000, 130: 224−232.

两步等离子体电解氧化陶瓷涂层的结构、腐蚀和力学行为

H. KHANMOHAMMADI, S. R. ALLAHKARAM, N. TOWHIDI

Mechanically Assisted Corrosion Laboratory, School of Metallurgy and Materials Engineering, College of Engineering, University of Tehran, P. O. Box 11155-4563 Tehran, Iran

摘　要：等离子体电解氧化(PEO)被认为是提高轻合金表面性能的一种低成本和环境友好的表面处理工艺。采用两步 PEO 法研究 Ti6Al14V 合金上陶瓷涂层的形成，并将该涂层样品的结构、电化学和力学性能与在碱性电解液中采用一步 PEO 法的样品进行比较。利用场发射扫描电镜(FESEM)和 X 射线衍射(XRD)技术对其结构性能进行表征。采用线性极化法进行电化学研究，并使用 Knoop 显微硬度和纳米压痕法研究其力学性能。结果表明，第二步电解氧化使涂层表面孔隙率和平均孔径都增大，两步法导致涂层厚度从 12.5 增加到 13.0 μm。电化学测试结果表明，第二步导致极化电阻从 1800.2 下降到 412.5 kΩ/cm^2，保护效率从 97.8%降至 90.5%。纳米压痕结果表明，在酸性电解液中采用第二步加工工艺后，PEO 涂层变得更加柔软，但韧性更大。

关键词：等离子体电解氧化；显微结构；腐蚀；纳米压痕

(Edited by Xiang-qun LI)